# Discovery of a Highly Neutronized Ejecta Clump in the Type Ia Supernova Remnant 3C 397

Yuken Ohshiro[1,2], Hiroya Yamaguchi[2,1] , Shing-Chi Leung[3] , Ken'ichi Nomoto[4] , Toshiki Sato[5] , Takaaki Tanaka[6] , Hiromichi Okon[7], Robert Fisher[8,9,10] , Robert Petre[11] , and Brian J. Williams[11]

[1] Department of Physics, Graduate School of Science, The University of Tokyo, 7-3-1 Hongo, Bunkyo-ku, Tokyo 113-0033, Japan
ohshiro-yuken@g.ecc.u-tokyo.ac.jp
[2] Institute of Space and Astronautical Science (ISAS), Japan Aerospace Exploration Agency (JAXA), 3-1-1 Yoshinodai, Chuo-ku, Sagamihara, Kanagawa 252-5210, Japan
[3] TAPIR, Walter Burke Institute for Theoretical Physics, Mailcode 350-17, Caltech, Pasadena, CA 91125, USA
[4] Kavli Institute for the Physics and Mathematics of the Universe (WPI), The University of Tokyo, Kashiwa, Chiba 277-8583, Japan
[5] Department of Physics, Rikkyo University, 3-34-1 Nishi Ikebukuro, Toshima-ku, Tokyo 171-8501, Japan
[6] Department of Physics, Konan University, 8-9-1 Okamoto, Higashinada, Kobe, Hyogo 658-8501, Japan
[7] Center for Astrophysics | Harvard & Smithsonian, 60 Garden Street, Cambridge, MA 02138, USA
[8] Department of Physics, University of Massachusetts Dartmouth, 285 Old Westport Road, North Dartmouth, MA 02740, USA
[9] Institute for Theory and Computation, Harvard-Smithsonian Center for Astrophysics, 60 Garden Street, Cambridge, MA 02138, USA
[10] Kavli Institute for Theoretical Physics, Kohn Hall, University of California at Santa Barbara, Santa Barbara, CA 93106, USA
[11] NASA Goddard Space Flight Center, Code 662, Greenbelt, MD 20771, USA
Received 2021 April 2; revised 2021 May 5; accepted 2021 May 8; published 2021 June 4

## Abstract

The supernova remnant (SNR) 3C 397 is thought to originate from a Type Ia supernova (SN Ia) explosion of a near-Chandrasekhar-mass ($M_{Ch}$) progenitor, based on the enhanced abundances of Mn and Ni revealed by previous X-ray study with Suzaku. Here we report follow-up XMM-Newton observations of this SNR, conducted with the aim of investigating the detailed spatial distribution of the Fe-peak elements. We have discovered an ejecta clump with extremely high abundances of Ti and Cr, in addition to Mn, Fe, and Ni, in the southern part of the SNR. The Fe mass of this ejecta clump is estimated to be $\sim$0.06 $M_{\odot}$, under the assumption of a typical Fe yield for SNe Ia (i.e., $\sim$0.8 $M_{\odot}$). The observed mass ratios among the Fe-peak elements and Ti require substantial neutronization that is achieved only in the innermost regions of a near-$M_{Ch}$ SN Ia with a central density of $\rho_c \sim 5 \times 10^9$ g cm$^{-3}$, significantly higher than typically assumed for standard near-$M_{Ch}$ SNe Ia ($\rho_c \sim 2 \times 10^9$ g cm$^{-3}$). The overproduction of the neutron-rich isotopes (e.g., $^{50}$Ti and $^{54}$Cr) is significant in such high-$\rho_c$ SNe Ia, with respect to the solar composition. Therefore, if 3C 397 is a typical high-$\rho_c$ near-$M_{Ch}$ SN Ia remnant, the solar abundances of these isotopes could be reproduced by the mixture of the high- and low-$\rho_c$ near-$M_{Ch}$ and sub-$M_{Ch}$ Type Ia events, with $\lesssim$20% being high-$\rho_c$ near-$M_{Ch}$.

*Unified Astronomy Thesaurus concepts:* Supernova remnants (1667)

## 1. Introduction

Thermonuclear explosions of carbon–oxygen white dwarfs (WDs), or Type Ia supernovae (SNe Ia), are important astrophysical phenomena, because of their roles as standardizable candles for cosmology (e.g., Phillips 1993) and major sources of Fe in the cosmic chemical enrichment (e.g., Kobayashi et al. 2020). Despite decades of intense effort, many properties of SNe Ia, including how their progenitors evolve and explode, remain unsolved (e.g., Maeda & Terada 2016). Given the relative uniformity in their observed properties, SNe Ia were formerly thought to originate always from near-Chandrasekhar-mass ($M_{Ch}$) WDs that had grown via mass accretion from their binary companion (e.g., Nomoto et al. 1984). However, recent theoretical and observational work has provided many pieces of evidence in favor of sub-$M_{Ch}$ progenitors as the major contributors to SNe Ia (e.g., Ruiter et al. 2009; Badenes & Maoz 2012; but see Hachisu et al. 2012 and Nomoto & Leung 2018 for counter arguments). In particular, element composition of several dwarf galaxies requires sub-Mch be dominant (McWilliam et al. 2018; Kirby et al. 2019).

Nevertheless, explosions of near-$M_{Ch}$ WDs are still necessary from the perspective of the chemical evolution in the Milky Way (e.g., Seitenzahl et al. 2013a; Kobayashi et al. 2020; Palla 2021) and galaxy clusters (e.g., Mernier et al. 2016; Hitomi Collaboration 2017), and even evolved dwarf spheroidal galaxies (de los Reyes et al. 2020). This is because efficient production of neutron-rich

isotopes of the Fe-peak elements, such as $^{54}$Cr, $^{55}$Mn, and $^{58}$Ni, require electron capture processes that take place only in the dense core of near-$M_{Ch}$ SNe Ia (e.g., Leung & Nomoto 2018, 2020), and the contributions of sub-$M_{Ch}$ SNe Ia cannot account for the observed abundances of these species. Evidence of these neutron-rich isotopes has been searched for in the late-time optical/infrared light curves of individual SN Ia events (e.g., Dimitriadis et al. 2017; Maguire et al. 2018). It is also suggested that future X-ray observations of nearby SNe Ia will be capable of detecting Mn K$\alpha$ lines from the decay of $^{55}$Fe, providing a powerful diagnostic for distinguishing between near-$M_{Ch}$ and sub-$M_{Ch}$ explosions (Seitenzahl et al. 2015; but see also Lach et al. 2020 and Gronow et al. 2021, who argued that solar or supersolar Mn/Fe ratios can be achieved by sub-$M_{Ch}$ explosions as well).

Observations of supernova remnants (SNRs) offer a complementary approach for constraining SN Ia progenitor mass and density. Although their X-ray spectra of Type Ia SNRs do not distinguish among isotopes of each element, mass ratios among the Fe-peak elements in the ejecta can be accurately measured, since the plasma is optically thin and physics of dominant atomic processes is relatively well understood. In fact, Suzaku observations of the SN Ia remnant 3C 397 detected strong K-shell fluorescence from the Fe-peak elements, and revealed that the observed mass ratios of Mn/Fe and Ni/Fe require substantial contributions from the electron capture elements, thereby ruling

out the sub-$M_{\rm Ch}$ scenario for this specific SNR (Yamaguchi et al. 2015).

Following the observational result with Suzaku, Dave et al. (2017) and Leung & Nomoto (2018) theoretically investigated the effect of the WD central density ($\rho_c$) on the resulting nucleosynthesis yields, and found that the mass ratios among the Fe-peak elements observed in 3C 397 can be reproduced by an explosion of a near-$M_{\rm Ch}$ WD with a central density of $\rho_c \approx 5 \times 10^9$ g cm$^{-3}$, significantly higher than usually assumed in models of "standard" near-$M_{\rm Ch}$ SNe Ia ( $\sim 2 \times 10^9$ g cm$^{-3}$; e.g., Iwamoto et al. 1999; Bravo & Martínez-Pinedo 2012). It is also notable that such high-density SN Ia models predict efficient production of $^{50}$Ti and $^{54}$Cr, in addition to $^{55}$Mn and $^{58}$Ni, due to the extremely high neutronization realized at the innermost region of the exploding WD (Dave et al. 2017; Leung & Nomoto 2018). Therefore, detection of ejecta with enhanced abundances of Ti and Cr would provide further evidence of the high-density near-$M_{\rm Ch}$ progenitor, and place a more stringent constraint on the central density (e.g., Sato et al. 2020).

In this Letter, we present XMM-Newton observations of 3C 397 conducted to use its superior angular resolution to Suzaku to search for highly neutronized ejecta. This SNR is located near the Galactic plane at a distance of ~8 kpc (Leahy & Ranasinghe 2016) and is well established as a middle-aged SN Ia remnant (Yamaguchi et al. 2014; Martínez-Rodríguez et al. 2020). Its angular size is about $5' \times 3'$. Because of the aim of this work, we focus exclusively on the imaging spectroscopic analysis of the K-shell emission from Ti and the Fe-peak elements in some small regions. The uncertainties quoted in the text and table and the error bars in the figures represent the $1\sigma$ confidence level.

## 2. Observation and Data Reduction

We conducted a deep observation of 3C 397 using the European Photon Imaging Camera (EPIC) on board XMM-Newton in 2018 October (Obs.ID: 0830450101). The EPIC consists of three charge-coupled devices, the MOS1, MOS2 (Turner et al. 2001), and pn (Strüder et al. 2001). The angular resolution of the telescopes is ~15″ (half-power diameter), good enough to resolve small spatial structures of 3C 397.

We reprocessed all the data using the `emchain` and `epchain` tasks (for MOS and pn, respectively) in version 18.0.0 of the XMM-Newton Science Analysis Software with the Current Calibration Files. Event selection was conducted based on the standard screening criteria. To eliminate data with high background rates, we filtered out observation periods when the count rate in the 0.2–12.0 keV band is higher than 8 cnt s$^{-1}$ (MOS1), 10 cnt s$^{-1}$ (MOS2), and 80 cnt s$^{-1}$ (pn). The resulting effective exposure is ~130 ks, more than 90% of the unfiltered exposure, for all the instruments.

## 3. Analysis and Results

Figure 1(a) shows an EPIC/MOS image of 3C 397 in the 6.4–6.7 keV band, corresponding to the Fe K$\alpha$ fluorescence from intermediately ionized Fe. There are two bright regions at the west and center of the SNR, as reported in previous work (Chen et al. 1999; Safi-Harb et al. 2005). We then investigate the spatial distribution of the other Fe-peak elements, and find that the morphology of the Cr K$\alpha$ emission is slightly different from that of the Fe K$\alpha$ emission (see Figure 1(a)). To highlight

this difference, we generate in Figure 1(b) a Cr-to-Fe flux ratio map by dividing the 5.4–5.7 keV image by the 6.4–6.7 keV image. The highest ratio is found in the south region.

For a more quantitative study, we extract EPIC spectra from the two representative regions, "South" and "West" in Figure 1. The former is where the highest Cr/Fe ratio is found, and the latter is where the surface brightness of both Fe K$\alpha$ and Cr K$\alpha$ emission is highest. Figures 2(a) and (b) show the background-subtracted spectra of the South and West, respectively. Since our primary goal is to determine the mass ratios among the Fe-peak elements and Ti, the following spectral analysis focuses on the 2.3–9 keV band so that we can model their K-shell emission as well as the underlying continuum emission adequately. The background data are taken from the outside of the SNR; the choice of background regions does not affect the following results significantly. In both spectra, K$\alpha$ lines of Cr, Mn, Fe, and Ni are clearly resolved. We confirm that the Cr K$\alpha$ emission is much stronger in the South than in the West, consistent with Figure 1(b). We also detect an emission feature around 4.7 keV in the South spectra, likely originating from the K$\alpha$ fluorescence of stable Ti.

The spectra of both regions are fitted with a model of optically thin thermal plasma in nonequilibrium ionization (NEI), using the XSPEC software version 12.11.00 (Arnaud 1996). The fitting is performed based on the $C$-statistic (Cash 1979) on unbinned spectra, although the spectra shown in Figure 2 are binned for clarity. For the foreground absorption, we introduce the Tuebingen-Boulder interstellar medium absorption (`TBabs`) model (Wilms et al. 2000) with the hydrogen column density ($N_{\rm H}$) fixed at $3 \times 10^{22}$ cm$^{-2}$ (Safi-Harb et al. 2005). We start fitting the spectra with a single NEI component, with free parameters of electron temperature ($kT_e$), ionization timescale ($n_e t$), normalization, and abundances of S, Ar, Ca, Ti, Cr, Mn, Fe, and Ni. This model fits the data well below 4 keV, but fails to reproduce the centroid of the emission lines of Ti and the Fe-peak elements or the continuum flux in >4 keV. We thus introduce another NEI component with different electron temperature and ionization timescale. The abundances of the heavy elements are also left independent between the two components. This addition significantly improves the c-stat values from 4406.02 to 4151.96 for the South and from 4475.16 to 4291.93 for the West. The results obtained for the two regions are summarized as follows: The low-$kT_e$ (~1 keV), high-$n_e t$ (~$10^{11}$ cm$^{-3}$ s) component reproduces the emission lines of S, Ar, and Ca, but does not significantly contribute to the emission of Ti, Cr, Mn, Fe, and Ni with their abundances consistent with zero. The high-$kT_e$ (~5 keV), low-$n_e t$ (~$3 \times 10^{10}$ cm$^{-3}$ s) component, on the other hand, yields extremely high ($\gtrsim 1000$ solar) abundances of Ti and the Fe-peak elements, implying that this component is dominated by these elements with no admixture of the lighter elements including H and He. We thus fix the abundances of Ti and the Fe-peak elements in the low-$kT_e$ component to zero. For the high-$kT_e$ component, we fix its Fe abundance to $1 \times 10^8$ solar (which mimics thermal emission from a pure-metal plasma) and allow the abundances of Ti, Cr, Mn, and Ni to vary freely, obtaining the best-fit results given in Table 1.

Finally, we convert the observed abundances to the mass ratios among the elements as follows:

$$\frac{M_i}{M_{\rm Fe}} = \frac{m_i}{m_{\rm Fe}} \frac{A_i}{A_{\rm Fe}} \left( \frac{n_i}{n_{\rm Fe}} \right)_\odot \; (i = {\rm Ti, Cr, Mn, Ni}),$$
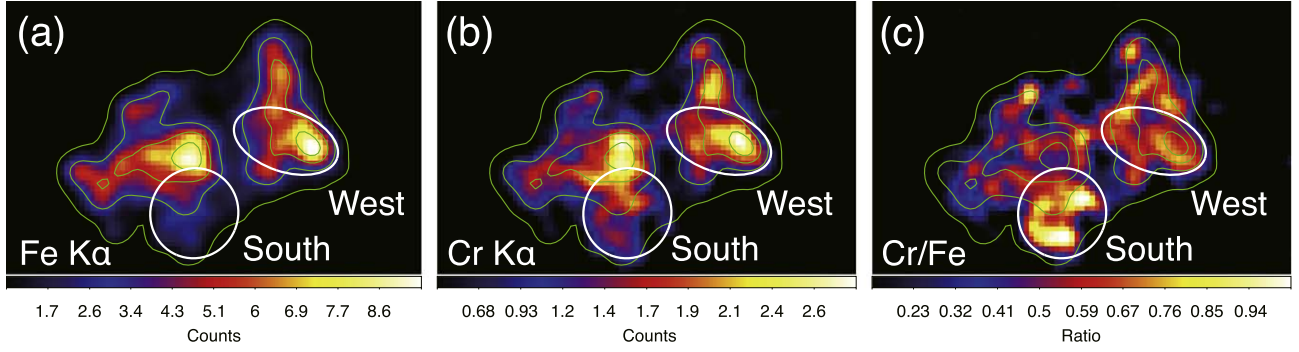
**Figure 1.** XMM-Newton/EPIC MOS images of the SNR 3C 397 in the (a) Fe Kα (6.4–6.7 keV) and (b) Cr Kα (5.4–5.7 keV) bands. (c) Spatial distribution of the flux ratio between the Cr Kα (5.4–5.7 keV) and Fe Kα (6.4–6.7 keV) emission. The overplotted contours in (b) and (c) are the Fe Kα flux image (same as panel (a)). The white ellipses indicate where the spectra shown in Figure 2 are extracted.
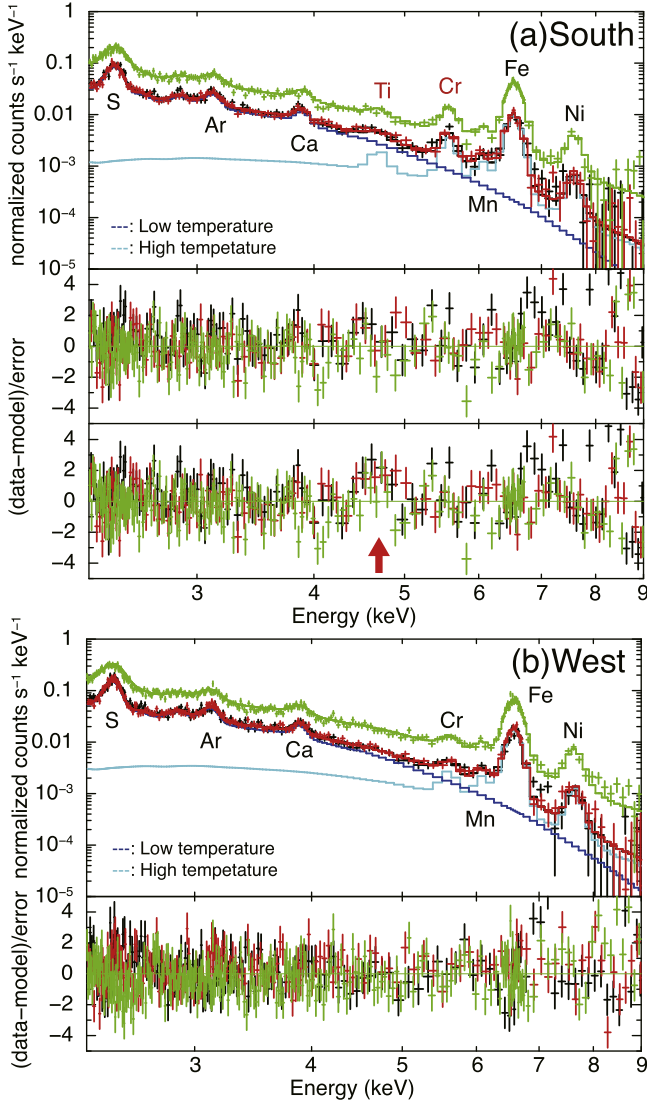


**Figure 2.** EPIC spectra in the 2.3–9.0 keV band extracted from the (a) South and (b) West regions given in Figure 1. Black, red, and green are MOS1, MOS2, and pn, respectively. The best-fit models for the low- and high-temperature components are given as blue and cyan lines, respectively. The bottom window of panel (a) shows the residuals from the best-fit model without Ti Kα emission, where the significant excess in the data is found around 4.7 keV (red arrow).

where $m_i$ is the atomic weight, $A_i$ is the observed abundance (Table 1), and $(n_i/n_{Fe})_\odot$ is the elemental number ratio in the solar abundance of Anders & Grevesse (1989). The resulting

**Table 1**
The Best-fit Parameters from Model Fitting and Derived Mass Ratios

| Region | South | West |
|---|---|---|
| Low-temperature Component | | |
| $kT_e$ (keV) | $1.14^{+0.06}_{-0.18}$ | $1.30^{+0.03}_{-0.06}$ |
| $n_e t$ ($10^{11}$ cm$^{-3}$ s) | $2.2^{+0.5}_{-0.5}$ | $1.2^{+0.2}_{-0.1}$ |
| $n_e n_H V^a$ ($10^{57}$ cm$^{-3}$) | $4.9^{+0.9}_{-0.3}$ | $7.0^{+0.3}_{-0.3}$ |
| S [solar] | $1.15^{+0.06}_{-0.06}$ | $1.19^{+0.07}_{-0.05}$ |
| Ar [solar] | $0.89^{+0.13}_{-0.10}$ | $1.03^{+0.09}_{-0.07}$ |
| Ca [solar] | $1.55^{+0.20}_{-0.19}$ | $1.83^{+0.22}_{-0.18}$ |
| High-temperature Component | | |
| $kT_e$ (keV) | $4.6^{+1.4}_{-1.8}$ | $3.4^{+0.3}_{-0.6}$ |
| $n_e t$ ($10^{10}$ cm$^{-3}$ s) | $2.9^{+0.7}_{-0.2}$ | $5.1^{+0.7}_{-0.1}$ |
| $n_e n_H V^a$ ($10^{49}$ cm$^{-3}$) | $4.0^{+4.6}_{-1.1}$ | $8.5^{+3.0}_{-0.9}$ |
| Velocity$^b$ ($10^3$ km s$^{-1}$) | $2.8^{+0.3}_{-0.3}$ | $2.7^{+0.2}_{-0.2}$ |
| Ti [$10^8$solar] | $8.0^{+2.2}_{-2.0}$ | $<0.9$ |
| Cr [$10^8$solar] | $11.4^{+0.1}_{-0.1}$ | $3.6^{+0.5}_{-0.4}$ |
| Mn [$10^8$solar] | $9.8^{+1.7}_{-1.7}$ | $9.7^{+1.2}_{-1.2}$ |
| Fe [$10^8$solar] | 1.0 (fixed) | 1.0 (fixed) |
| Ni [$10^8$solar] | $4.5^{+1.7}_{-0.7}$ | $6.8^{+1.3}_{-0.7}$ |
| Statistic | | |
| cstat | 4151.96 | 4291.93 |
| d.o.f. | 4001 | 4002 |
| Mass Ratio | | |
| Ti/Fe | $0.014^{+0.004}_{-0.004}$ | $<0.002$ |
| Cr/Fe | $0.106^{+0.011}_{-0.009}$ | $0.034^{+0.004}_{-0.004}$ |
| Mn/Fe | $0.051^{+0.009}_{-0.009}$ | $0.050^{+0.006}_{-0.006}$ |
| Ni/Fe | $0.18^{+0.07}_{-0.03}$ | $0.27^{+0.05}_{-0.03}$ |

**Notes.**
$^a$ The volume emission measure, where $n_e$ is the electron density, $n_H$ is the hydrogen density, and $V$ is the volume of the emission region.
$^b$ Velocity dispersion in the line of sight for the Doppler broadening of the emission lines.

mass ratios are also given in Table 1. In this conversion, we have assumed the average atomic weight in the solar system (i.e., $m_{Ti} = 47.9$, $m_{Cr} = 52.0$, $m_{Mn} = 54.9$, $m_{Fe} = 55.8$, and $m_{Ni} = 58.7$). Although the isotope ratios expected for SN Ia yields are not identical to the solar composition (see Section 4), the difference between them is negligibly small (e.g., $\lesssim4\%$ for Ti) compared to the statistical uncertainty.

## 4. Interpretation and Discussion

Thanks to the excellent angular resolution and sensitivity of the XMM-Newton/EPIC, we have succeeded in spatially resolving an ejecta clump with an enhanced Cr abundance at the South of SNR 3C 397. Its Cr/Fe mass ratio is about three times higher than that in the West as well as the previous Suzaku measurement for the entire SNR (Yamaguchi et al. 2015). The spectra also suggest that this ejecta clump has an extremely high abundance of stable Ti. To our knowledge, this is the first detection of stable Ti from this SNR and the second after Tycho's SNR (Miceli et al. 2015) among Type Ia SNRs.[12] Note however that the detection in Tycho's SNR has been disputed by Yamaguchi et al. (2017) and Sato et al. (2020). This is because the centroid energy of the detected line ($\sim$4.9 keV) corresponds to the Ly$\alpha$ emission of H-like Ti, is unnaturally higher than expected for the plasma condition in Tycho's SNR. In our results, K-shell lines of Ti and the Fe-peak elements are all reproduced by a single plasma component, indicating the robustness of the Ti line detection.

The Fe K$\alpha$ flux ($F$) of the ejecta clump is estimated to be $1.7 \times 10^{-13}$ erg cm$^{-2}$ s$^{-1}$, which is 13% of the Fe K$\alpha$ flux from the entire SNR ($1.3 \times 10^{-12}$ erg cm$^{-2}$ s$^{-1}$). The observed solid angle ($\Omega$) of the ejecta clump is $1.5 \times 10^{-7}$ sr, about 12% of the solid angle subtended by the entire SNR. For a pure-metal plasma, the relationship between the Fe mass ($M_{\mathrm{Fe}}$) and $F$ is given as $M_{\mathrm{Fe}} \propto (F \cdot V)^{1/2} \sim F^{1/2} \cdot \Omega^{3/4}$ (where $V$ is the plasma volume, within which uniform density distribution is assumed). Therefore, we estimate the Fe mass in the ejecta clump to be $\sim$7% of the total Fe ejecta mass, corresponding to $\sim$0.06 $M_{\odot}$, under an assumption of a typical SN Ia Fe yield (i.e., $\sim$0.8 $M_{\odot}$).

Our spectral analysis indicates that Ti and all the Fe-peak elements compose a single (high-$kT_e$) plasma component, suggesting that these elements are generated by a common nucleosynthesis regime. In the case of near-$M_{\mathrm{Ch}}$ SNe Ia, Ti and Cr (or their parent nuclei) are synthesized in either incomplete Si burning or neutron-rich nuclear statistical equilibrium (n-rich NSE). The former takes place in the relatively low-temperature ($T \sim 5 \times 10^9$ K) and low-density ($\rho \sim 10^7$ g cm$^{-3}$) environment and produces $^{48}$Cr and $^{52}$Fe via $\alpha$-processes, which eventually decay into $^{48}$Ti and $^{52}$Cr, respectively. However, production of stable Ni requires higher temperature and density (e.g., Iwamoto et al. 1999). The n-rich NSE, on the other hand, takes place in a high-temperature ($T \gtrsim 5.5 \times 10^9$ K) and high-density ($\rho \gtrsim 3 \times 10^8$ g cm$^{-3}$) environment and directly produces the neutron-rich isotopes of all the elements found in the high-$kT_e$ component (e.g., $^{50}$Ti, $^{52}$Cr, $^{54}$Cr, $^{55}$Mn, $^{54}$Fe, $^{56}$Fe, $^{58}$Ni). Therefore, we conclude that the ejecta clump in the 3C 397 South is an n-rich NSE product originating from the dense core of the near-$M_{\mathrm{Ch}}$ progenitor.

It is theoretically suggested that efficient production of stable Ti and Cr in SNe Ia is achieved only when the WD central density is sufficiently high ($\rho_c \gtrsim 3 \times 10^9$ g cm$^{-3}$). This is illustrated in Figure 3, numerical calculations of SN Ia nucleosynthesis with different $\rho_c$ assumed (Leung & Nomoto 2018). These models are based on two-dimensional hydrodynamical calculations of the delayed-detonation explosion (e.g., Khokhlov 1991) of a near-$M_{\mathrm{Ch}}$ WD with the solar metallicity. Note that, in the n-rich

NSE, the metallicity effect on the resulting nucleosynthesis yields is negligible (e.g., Yamaguchi et al. 2015). The models assume central ignition of the carbon deflagration and a detonation transition density of $\sim$2 $\times 10^7$ g cm$^{-3}$. Figures 3(a) and (b) show Ti/Fe mass ratios plotted against the density when each tracer particle achieves the maximum temperature during the nuclear burning, ($\rho_{T_{\mathrm{Max}}}$), for the cases of $\rho_c = 1 \times 10^9$ g cm$^{-3}$ (low density) and $\rho_c = 5 \times 10^9$ g cm$^{-3}$ (high density), respectively. The mass ratio observed in the 3C 397 South region is also indicated with the red area. Similar comparisons for the Cr/Fe mass ratios are given in Figures 3(c) and (d) for the low- and high-density cases, respectively. It is confirmed that only the innermost ejecta in the high-density case achieve the observed mass ratios of $M_{\mathrm{Ti}}/M_{\mathrm{Fe}} \sim 0.01$ and $M_{\mathrm{Cr}}/M_{\mathrm{Fe}} \sim 0.1$.

At lower densities around $1 \times 10^9$ g cm$^{-3}$, the neutronized nucleosynthesis products are dominated by $^{58}$Ni, since the neutron excess in the NSE is not high enough to produce stable Ti and Cr. For this reason, the mass ratios of Ti/Ni and Cr/Ni at the innermost part offer the most sensitive indicators of the central density of near-$M_{\mathrm{Ch}}$ WDs (e.g., Leung & Nomoto 2018; Mori et al. 2018).

In Figure 4, we plot these mass ratios (and $M_{\mathrm{Mn}}/M_{\mathrm{Ni}}$) as a function of $\rho_c$, predicted for the innermost ejecta by the models of Leung & Nomoto (2018). Here we define the "innermost ejecta" as the ejecta in the highest $\rho_{T_{\mathrm{Max}}}$ regions whose integrated Fe mass is 7% of the total Fe yield (or $M_{\mathrm{Fe}} \sim 0.06\,M_{\odot}$), so that we can directly compare the theoretical predictions with the observed mass ratios for 3C 397 South ejecta clump. We find that all the ratios require a central density of $>3 \times 10^9$ g cm$^{-3}$. In particular, the Ti/Fe ratio indicates $\rho_c \approx 5 \times 10^9$ g cm$^{-3}$, suggesting strongly the high-density scenario for the progenitor of 3C 397. We note that the mass ratios given in Figure 4 do not point toward a single value of $\rho_c$. However, in addition to the white dwarf central density, the nucleosynthetic abundances depend on a larger parameter space, including the number of ignition kernels and the detonation transition density among others. Also, in the accreting WD models of SNe Ia, $\rho_c$ depends on the accretion rate, the initial mass of the WD, and the angular momentum of the WD (Nomoto 1982; Benvenuto et al. 2015). It would be important to clarify the evolutionary origin of such high $\rho_c$ near-$M_{\mathrm{Ch}}$ SNe Ia as 3C 397 in future studies.

Martínez-Rodríguez et al. (2017) argued that the predicted mass ratio of Ca/S was sensitive to the progenitor metallicity and claimed a supersolar metallicity for the progenitor of 3C 397. We have also investigated the nucleosynthesis calculations of Dave et al. (2017) and Leung & Nomoto (2018), and confirmed that, regardless of central density, the predicted Ca/S mass ratios for the entire ejecta show a metallicity dependence similar to that reported in Martínez-Rodríguez et al. (2017). In contrast, the yields of the neutron-rich Fe-peak elements (i.e., Ti and Cr) in the innermost ejecta are sensitive only to the central density (Leung & Nomoto 2018). Therefore, in principle, both progenitor metallicity and central density can be independently constrained using the mass ratios of these diagnostic elements measured based on spatially resolved spectroscopy.

Interestingly, the neutronized ejecta clump is located at the southern outermost part of the SNR (see Figure 1), despite its plausible origin of the densest WD core. This is, in fact, qualitatively consistent with predictions of multidimensional hydrodynamical calculations for an asymmetric SN Ia that involve delayed detonation (e.g., Maeda et al. 2010; Seitenzahl et al. 2013b). In these models, the nuclear burning that takes

---

[12] Emission from stable Ti has recently been detected in a core-collapse SNR, Cassiopeia A (Sato et al. 2021). This emission is thought to originate predominantly from $^{48}$Ti (a major product of $\alpha$-rich freeze out), whereas the stable Ti detected in 3C 397 is likely dominated by $^{50}$Ti.
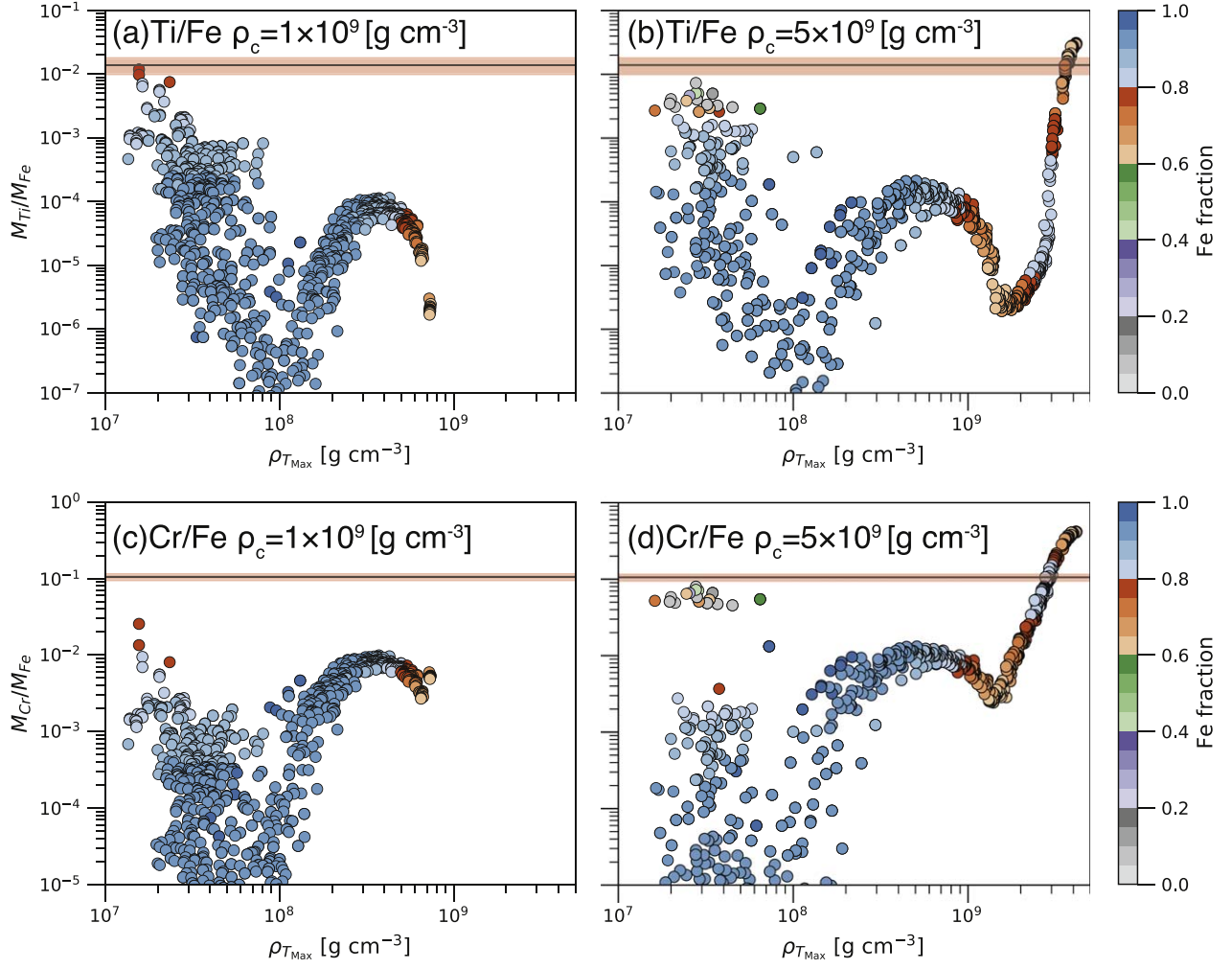
**Figure 3.** Top: relationship between the Ti/Fe mass ratio and $\rho_{T_{\mathrm{Max}}}$ (the density when each tracer particle achieves the maximum temperature) predicted by the delayed-detonation near-$M_{\mathrm{Ch}}$ SN Ia models with (a) $\rho_c = 1 \times 10^9$ g cm$^{-3}$ and (b) $\rho_c = 5 \times 10^9$ g cm$^{-3}$ (Leung & Nomoto 2018). Only the particles that satisfy $T_{\mathrm{Max}} \geqslant 5.5 \times 10^9$ K are plotted. The Fe fraction in each particle is indicated by color. The observed mass ratio is indicated with the horizontal lines (best-fit) and red regions ($1\sigma$ statistical uncertainty). Bottom: same as the top panels, but for the Cr/Fe mass ratio. Panels (c) and (d) are for $\rho_c = 1 \times 10^9$ g cm$^{-3}$ and $\rho_c = 5 \times 10^9$ g cm$^{-3}$, respectively.
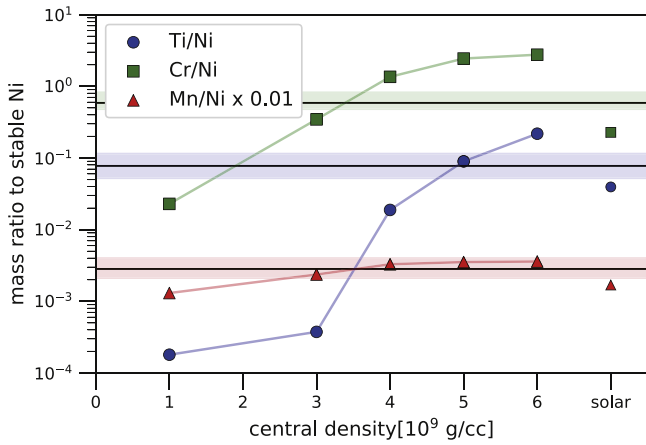


**Figure 4.** Predicted mass ratios of Ti/Ni (blue), Cr/Ni (green), and Mn/Ni (red) in the innermost ejecta (see the text) as a function of the WD central density. The observed mass ratios are indicated with the horizontal lines and colored areas. The solar values of Lodders (2003) are also plotted at the rightmost for comparison.

place during the initial deflagration phase makes the burnt materials hotter and less dense than the surrounding unburnt materials, leading to the buoyant rise of the deflagration ash (i.e., n-rich NSE products) to the WD surface.

As mentioned in Section 1, the nucleosynthesis that occurs in sub-$M_{\mathrm{Ch}}$ Type Ia SNe does not produce the observed abundances of Fe-peak isotopes; a contribution from near-$M_{\mathrm{Ch}}$ explosions is needed (e.g., Seitenzahl et al. 2013a; Hitomi Collaboration 2017; Kobayashi et al. 2020). In taking into account nucleosynthesis of near-$M_{\mathrm{Ch}}$ SNe Ia, we should note that the abundance ratios of Fe-peak elements depend sensitively on $\rho_c$ of the WD. For $\rho_c \sim 2 \times 10^9$ g cm$^{-3}$ (low-$\rho_c$), the abundance pattern is close to solar, while for $\rho_c \approx 5 \times 10^9$ g cm$^{-3}$ (high-$\rho_c$), the neutron-rich isotopes are overproduced with respect to the solar ratios. Suppose that there are three types of SNe Ia, i.e., (1) high-$\rho_c$ near-$M_{\mathrm{Ch}}$ SNe Ia, (2) low-$\rho_c$ near-$M_{\mathrm{Ch}}$ SNe Ia, and (3) sub-$M_{\mathrm{Ch}}$ SNe Ia. Then the ratios between these three types are subject to the nucleosynthesis yields of each SN type. If 3C 397 is the remnant of a typical high-$\rho_c$ near-$M_{\mathrm{Ch}}$ SN Ia, we can obtain more quantitative constraints on the frequency of such SN Ia by applying the

nucleosynthesis yields of the $\rho_c = 5 \times 10^9$ g cm$^{-3}$ model (Leung & Nomoto 2018). This model overproduces the neutron-rich isotopes with the ratios of $^{50}$Ti/$^{56}$Fe and $^{54}$Cr/$^{56}$Fe being 5.3 and 18.6 times the solar ratio, respectively (Leung & Nomoto 2018). On the other hand, these ratios are negligibly small in the low-$\rho_c$ near-$M_{Ch}$ SN Ia and sub-$M_{Ch}$ SN Ia, so that these types of SNe Ia contribute to dilution of neutron-rich isotopes by producing $\sim 0.8 M_\odot$ Fe. Thus, the solar abundances of these isotopes are reproduced by the mixture of the high-$\rho_c$ near-$M_{Ch}$ SNe Ia for $\lesssim 20\%$, and the other SNe Ia for the rest. To obtain further constraints on the ratios among three types of SNe Ia needs to consider additional elements.

It is worth noting that a departure from the solar composition in the neutron-rich isotopic abundances (e.g., $^{48}$Ca, $^{50}$Ti, $^{54}$Cr) is commonly seen in carbonaceous chondrites meteorites (e.g., Dauphas et al. 2010, 2014; Warren 2011; Nittler et al. 2018). These meteorites are thought to be composed of presolar grains that were injected by nearby supernovae to the protosolar disk. The literature argued that the isotopic anomalies observed in the carbonaceous chondrites could be explained by either high-density ($\rho_c \gtrsim 5 \times 10^9$ g cm$^{-3}$) SNe Ia or electron capture supernovae (ECSNe; Nomoto & Leung 2017), but no determination has been made. Our result potentially helps distinguish between the two scenarios, since it offers evidence for the existence of high-density SNe Ia. It is also notable that Nittler et al. (2018) reported an extremely high abundance of $^{54}$Cr in the smallest ($\lesssim 80$ nm) grains. Theoretically, such small grains tend to be produced by SNe Ia (Nozawa et al. 2011), qualitatively supporting the SNe Ia scenario for the origin of the isotopic anomalies.

## 5. Conclusions

We have presented an imaging spectroscopic study of the Fe-peak elements in SNR 3C 397, using a the deep XMM-Newton observation conducted in 2018. An enhanced abundance of Cr is found in an ejecta clump in the southern part of the SNR, where we have also detected K-shell emission from stable Ti. The mass ratios of Ti/Fe, Cr/Fe, Mn/Fe, and Ni/Fe are obtained to be $0.014^{+0.004}_{-0.004}$, $0.106^{+0.011}_{-0.009}$, $0.050^{+0.009}_{-0.009}$, and $0.18^{+0.07}_{-0.03}$, respectively. The creation of elements with these abundances requires substantial neutronization that can be achieved only in the innermost regions of a near-$M_{Ch}$ SN Ia with a central density of $4$–$5 \times 10^9$ g cm$^{-3}$. The ejecta clump location implies that the n-rich NSE products buoyantly rose to the stellar surface during the initial deflagration phase. If a 3C 397-like SN Ia is typical of high-$\rho_c$ near-$M_{Ch}$ explosion, the solar abundance ratios of $^{50}$Ti/$^{56}$Fe and $^{54}$Cr/$^{56}$Fe can be reasonably explained by a combination of the high-$\rho_c$ near-$M_{Ch}$, and the low-$\rho_c$ near-$M_{Ch}$ and sub-$M_{Ch}$ Type Ia events, with $\lesssim 20\%$ being high-$\rho_c$ near-$M_{Ch}$. Our results may also help identify the origin of isotopic anomalies observed in presolar grains that compose carbonaceous chondrites.

## ORCID iDs

Hiroya Yamaguchi ● https://orcid.org/0000-0002-5092-6085
Shing-Chi Leung ● https://orcid.org/0000-0002-4972-3803
Ken'ichi Nomoto ● https://orcid.org/0000-0001-9553-0685
Toshiki Sato ● https://orcid.org/0000-0001-9267-1693
Takaaki Tanaka ● https://orcid.org/0000-0002-4383-0368
Robert Fisher ● https://orcid.org/0000-0001-8077-7255
Robert Petre ● https://orcid.org/0000-0003-3850-2041
Brian J. Williams ● https://orcid.org/0000-0003-2063-381X

## References

Anders, E., & Grevesse, N. 1989, GeCoA, 53, 197
Arnaud, K. A. 1996, in ASP Conf. Ser. 101, Astronomical Data Analysis Software and Systems V, ed. G. H. Jacoby & J. Barnes (San Francisco, CA: ASP), 17
Badenes, C., & Maoz, D. 2012, ApJL, 749, L11
Benvenuto, O. G., Panei, J. A., Nomoto, K., Kitamura, H., & Hachisu, I. 2015, ApJL, 809, L6
Bravo, E., & Martínez-Pinedo, G. 2012, PhRvC, 85, 055805
Cash, W. 1979, ApJ, 228, 939
Chen, Y., Sun, M., Wang, Z.-R., & Yin, Q. F. 1999, ApJ, 520, 737
Dauphas, N., Chen, J. H., Zhang, J., et al. 2014, E&PSL, 407, 96
Dauphas, N., Remusat, L., Chen, J. H., et al. 2010, ApJ, 720, 1577
Dave, P., Kashyap, R., Fisher, R., et al. 2017, ApJ, 841, 58
de los Reyes, M. A. C., Kirby, E. N., Seitenzahl, I. R., & Shen, K. J. 2020, ApJ, 891, 85
Dimitriadis, G., Sullivan, M., Kerzendorf, W., et al. 2017, MNRAS, 468, 3798
Gronow, S., Cote, B., Lach, F., et al. 2021, A&A, submitted (arXiv:2103.14050)
Hachisu, I., Kato, M., & Nomoto, K. 2012, ApJL, 756, L4
Hitomi Collaboration 2017, Natur, 551, 478
Iwamoto, K., Brachwitz, F., Nomoto, K., et al. 1999, ApJS, 125, 439
Khokhlov, A. M. 1991, A&A, 245, 114
Kirby, E. N., Xie, J. L., Guo, R., et al. 2019, ApJ, 881, 45
Kobayashi, C., Leung, S.-C., & Nomoto, K. 2020, ApJ, 895, 138
Lach, F., Röpke, F. K., Seitenzahl, I. R., et al. 2020, A&A, 644, A118
Leahy, D. A., & Ranasinghe, S. 2016, ApJ, 817, 74
Leung, S.-C., & Nomoto, K. 2018, ApJ, 861, 143
Leung, S.-C., & Nomoto, K. 2020, ApJ, 888, 80
Lodders, K. 2003, ApJ, 591, 1220
Maeda, K., Röpke, F. K., Fink, M., et al. 2010, ApJ, 712, 624
Maeda, K., & Terada, Y. 2016, IJMPD, 25, 1630024
Maguire, K., Sim, S. A., Shingles, L., et al. 2018, MNRAS, 477, 3567
Martínez-Rodríguez, H., Badenes, C., Yamaguchi, H., et al. 2017, ApJ, 843, 35
Martínez-Rodríguez, H., Lopez, L. A., Auchettl, K., et al. 2020, MNRAS, submitted (arXiv:2006.08681)
McWilliam, A., Piro, A. L., Badenes, C., & Bravo, E. 2018, ApJ, 857, 97
Mernier, F., de Plaa, J., Pinto, C., et al. 2016, A&A, 595, A126
Miceli, M., Sciortino, S., Troja, E., & Orlando, S. 2015, ApJ, 805, 120
Mori, K., Famiano, M. A., Kajino, T., et al. 2018, ApJ, 863, 176
Nittler, L. R., Alexander, O'D., Liu, C. M., & Wang, J., N. 2018, ApJL, 856, L24
Nomoto, K. 1982, ApJ, 253, 798
Nomoto, K., & Leung, S.-C. 2017, in Handbook of Supernovae, ed. A. W. Alsabti & P. Murdin (Berlin: Springer), 483
Nomoto, K., & Leung, S.-C. 2018, SSRv, 214, 67
Nomoto, K., Thielemann, F.-K., & Yokoi, K. 1984, ApJ, 286, 644
Nozawa, T., Maeda, K., Kozasa, T., et al. 2011, ApJ, 736, 45
Palla, M. 2021, MNRAS, 503, 3216
Phillips, M. M. 1993, ApJL, 413, L105
Ruiter, A. J., Belczynski, K., & Fryer, C. 2009, ApJ, 699, 2026
Safi-Harb, S., Dubner, G., Petre, R., Holt, S. S., & Durouchoux, P. 2005, ApJ, 618, 321

Sato, T., Bravo, E., Badenes, C., et al. 2020, ApJ, 890, 104
Sato, T., Maeda, K., Nagataki, S., et al. 2021, Natur, 592, 537
Seitenzahl, I. R., Cescutti, G., Röpke, F. K., Ruiter, A. J., & Pakmor, R. 2013a, A&A, 559, L5
Seitenzahl, I. R., Ciaraldi-Schoolmann, F., Röpke, F. K., et al. 2013b, MNRAS, 429, 1156
Seitenzahl, I. R., Summa, A., Krauß, F., et al. 2015, MNRAS, 447, 1484

Strüder, L., Briel, U., Dennerl, K., et al. 2001, A&A, 365, L18
Turner, M. J. L., Abbey, A., Arnaud, M., et al. 2001, A&A, 365, L27
Warren, P. H. 2011, E&PSL, 311, 93
Wilms, J., Allen, A., & McCray, R. 2000, ApJ, 542, 914
Yamaguchi, H., Badenes, C., Foster, A. R., et al. 2015, ApJL, 801, L31
Yamaguchi, H., Badenes, C., Petre, R., et al. 2014, ApJL, 785, L27
Yamaguchi, H., Hughes, J. P., Badenes, C., et al. 2017, ApJ, 834, 124